ACSNANO

www.acsnano.org

ARTICLE

Helical Fiber Strain Sensors Based on Triboelectric Nanogenerators for Self-Powered Human Respiratory Monitoring

Chuan Ning,[#] Renwei Cheng,[#] Yang Jiang,[#] Feifan Sheng, Jia Yi, Shen Shen, Yihan Zhang, Xiao Peng, Kai Dong,[*] and Zhong Lin Wang[*]

Cite This: https://doi.org/10.1021/acsnano.1c09792

Read Online

ACCESS | Metrics & More | Article Recommendations | Supporting Information

ABSTRACT: **Respiration is a major vital sign, which can be used for early illness diagnosis and physiological monitoring. Wearable respiratory sensors present an exciting opportunity to monitor human respiratory behaviors in a real-time, noninvasive, and comfortable way. Among them, fiber-shaped triboelectric nanogenerators (FS-TENGs) are attractive for their comfort and high degree of freedom. However, the single-electrode FS-TENGs cannot respond to their own tensile strains, and the coaxial double-electrode FS-TENGs show low sensitivity to strain due to structural limitations. Here, a type of helical fiber strain sensor (HFSS) is developed, which can respond to tiny tensile strains. In addition, a smart wearable real-time respiratory monitoring system is developed based on the HFSSs, which can measure some key breathing parameters for disease prevention and medical diagnosis. An intelligent alarm can automatically call a preset mobile phone for help in response to respiratory behavior changes. This work provides an effective helical structure for fabricating highly sensitive strain sensors based on FS-TENGs and develops wearable self-powered real-time respiratory monitoring systems.**

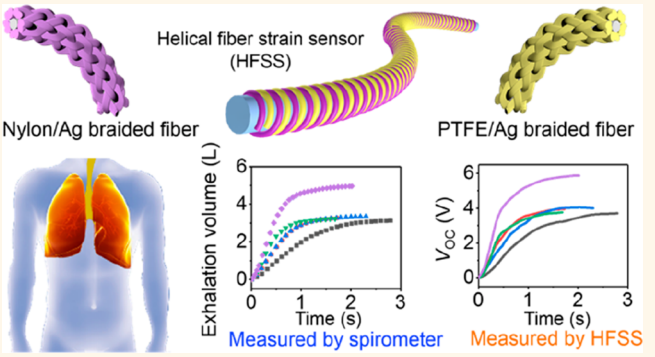

KEYWORDS: *fiber-shaped, strain sensing, helical structure, triboelectric nanogenerators, respiratory monitoring*

INTRODUCTION

Self-powered personalized physiological signal monitoring has attracted great interest due to the increasing demand for fitness monitoring, health assessment, and early disease alerts.[1−4] Respiration is one of the vital signs for human health monitoring, encompassing a great deal of physiological information about individual health as well as potential diseases.[5−7] Real-time respiratory monitoring can detect potential disease risks in time and even save lives.[8,9] However, most of the current respiratory monitoring methods, such as respiratory masks and endotracheal nostril intubation, are not suitable for carrying around and real-time monitoring due to their cumbersome devices, complex structure, uncomfortable use experience, and external power requirement.[10−12] Therefore, comfortable and wearable real-time respiratory monitoring systems are particularly important.

Triboelectric nanogenerators (TENGs), as an emerging technology for converting mechanical movement into electrical signals,[13−17] have been widely adopted for self-powered wearable physiological signal monitoring in recent years due to their low cost, flexible design, and excellent adaptability.[18−20] Among them, the fiber-shaped TENGs (FS-TENGs) have attracted wide attention due to their high degree of freedom and flexibility,[21−23] which can also be easily transformed from one-dimensional (1D) to two-dimensional (2D) or three-dimensional (3D) structures.[24−27] The 1D stretchable FS-TENGs usually adopt a single-electrode mode or coaxial two-electrode contact−separation mode.[21,28−30] The single-electrode FS-TENG requires contact with external objects to generate electrical signals and cannot respond to its stretching.[31−33] The inner and outer triboelectric layers of the coaxial double-electrode FS-TENG are arranged in parallel, and the FS-TENG needs to be stretched to a certain length to

Received: November 4, 2021
Accepted: January 26, 2022

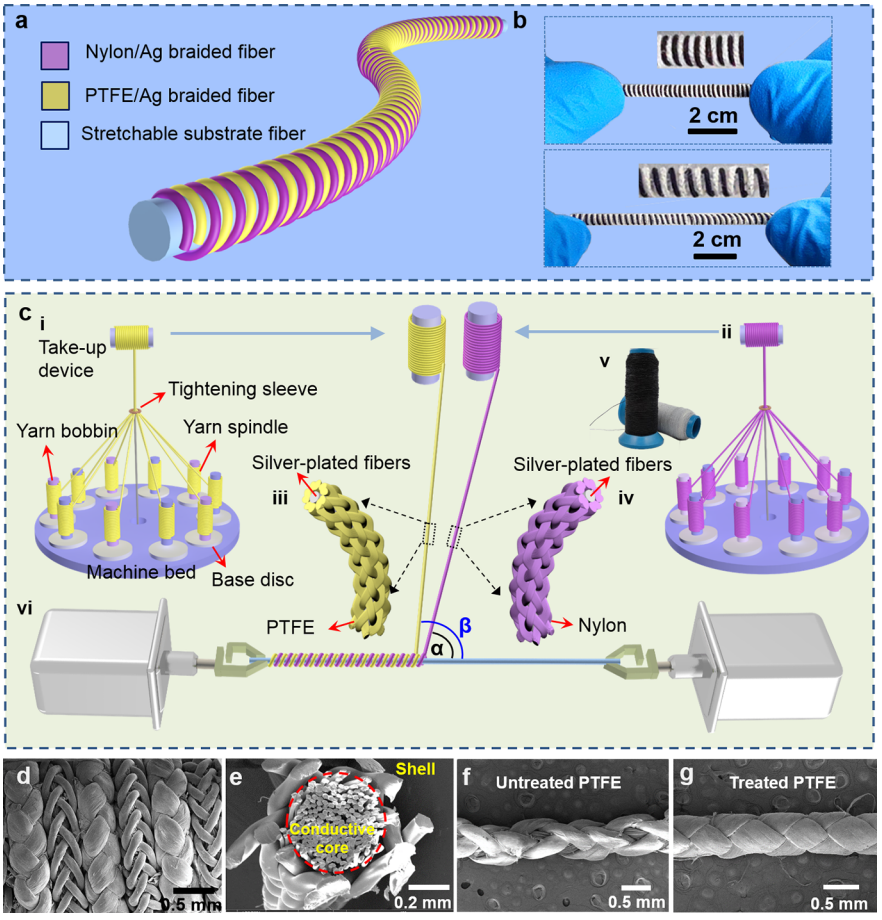

Figure 1. Structure design and fabrication process of the HFSSs. (a) Schematic structure diagram of the HFSS with helical structure. (b) Photographs of the HFSS under strains of 0% and 80%, respectively. (c) Fabrication process of the (i) PTFE/Ag braided fibers and (ii) nylon/Ag braided fibers. The core−shell fibers are made by a multiaxial fiber winding machine. Schematic illustration of (iii) PTFE/Ag braided fiber and (iv) nylon/Ag braided fiber. (v) Photograph of core−shell fibers made by the multiaxial fiber winding machine. (vi) Schematic diagram of the winding process of the two kinds of core−shell fibers. (d) SEM image of the HFSSs surface. (e) SEM image of the section of the core−shell fibers. PTFE/Ag braided fibers (f) based on untreated PTFE and (g) based on treated PTFE.

contact, which leads to low sensitivity to strain.[34−37] Therefore, the sensitivity of the existing FS-TENG is too low to meet the demand. One of the ways to improve sensitivity is to change the traditional structure.

In this paper, a type of helical fiber strain sensor (HFSS) is developed by designing a helical structure on a stretchable substrate fiber. Unlike other stretchable FS-TENGs,[21,36,37] the HFSSs take full advantage of their helical structure. Even with slight stretching, the state of contact between the two triboelectric layers [polytetrafluoroethylene (PTFE) and nylon] changes, resulting in an effective electrical signal. Therefore, HFSSs can respond to tiny tensile strains with a detection limit of less than 1%. In addition, compared with resistive, capacitive, and optical strain sensors, the triboelectric sensors are self-powered and do not need an external power supply in the process of signal acquisition.[38] The self-powered HFSSs are integrated into a chest strap and fastened below the thoracic cavity to monitor human respiration. It can be regularly stretched and contracted as the chest cavity expands/contracts. Through the calculation and processing of these electrical signals, some indicators such as human respiratory rate, forced vital capacity (FVC), forced expiratory volume in one second (FEV1), and peak expiratory flow (PEF) can be obtained. Moreover, a smart wearable real-time respiratory monitoring system is developed, which contains a smart spirometer and a self-powered intelligent alarm. The smart spirometer can quantify the volume of airflow per expiration and initially diagnose respiratory diseases. The intelligent alarm can automatically call a preset mobile phone for help when the subject stops breathing for more than 6 s. The system helps to assess the respiratory condition, detect potential disease risks, and even save lives, which shows great potential in personal respiratory health monitoring and smart wearable medical electronics.

RESULTS AND DISCUSSION

In this study, commercial silver-plated nylon fiber is selected as the electrode, considering its low cost and maturity in industrial production. PTFE fibers and nylon fibers are chosen as triboelectric materials. PTFE has high mechanical durability, inherent biocompatibility, and a strong ability to gain electrons. Nylon, a common wearable fiber, is a material that tends to lose electrons. As shown in Figure 1a and d, the PTFE winding Ag-coated nylon fibers (PTFE/Ag braided fibers) and the nylon winding Ag-coated nylon fibers (nylon/Ag braided fibers) are alternately wound around a stretchable substrate fiber to form the HFSSs. The contact−separation of the two triboelectric layers (PTFE and nylon) can be implemented by

https://doi.org/10.1021/acsnano.1c09792
ACS Nano XXXX, XXX, XXX−XXX

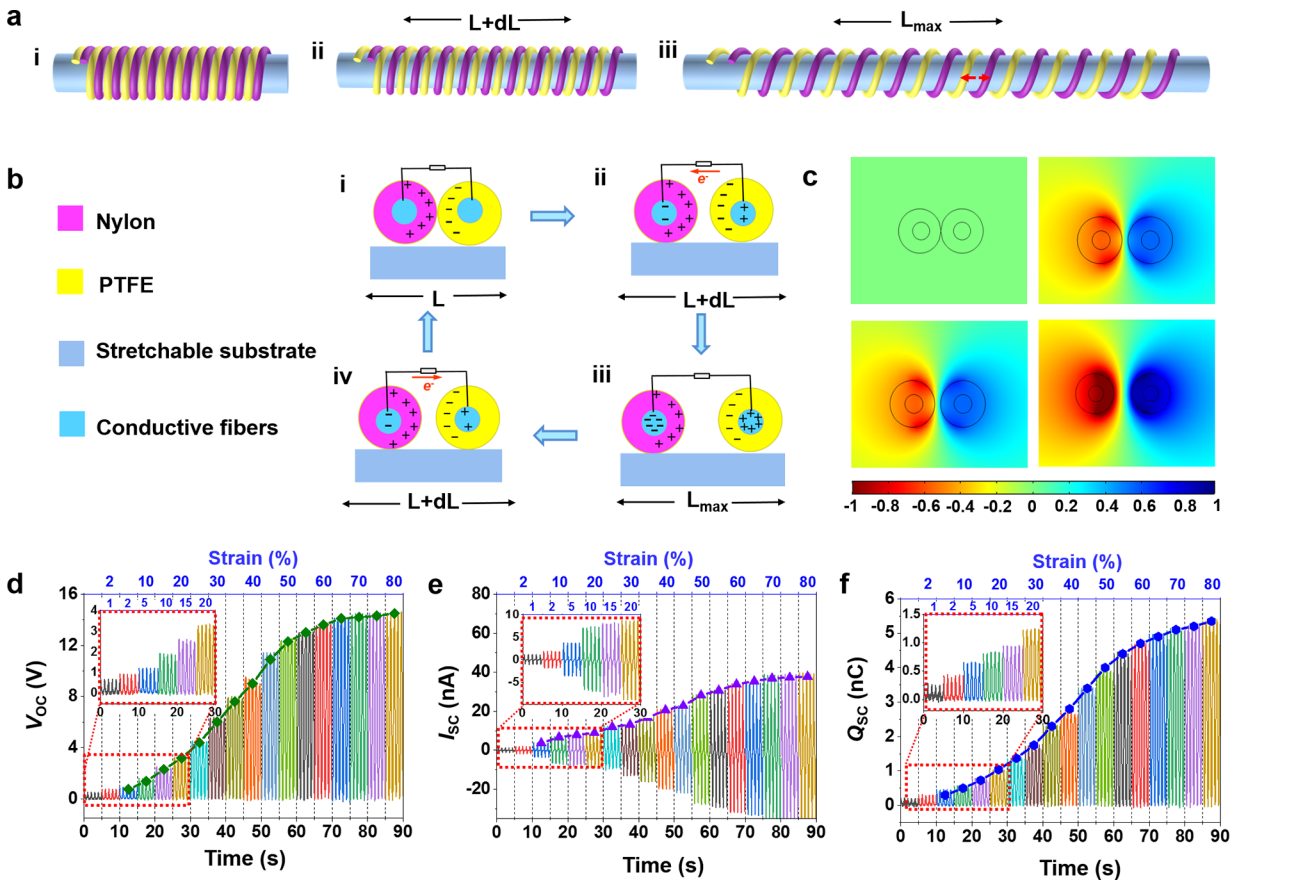

Figure 2. Working principle and the electrical output under different stretching strain of the HFSSs. (a) Structural illustrations of the HFSSs at different states: (i) side view without deformation; (ii) detached windings under tension; (iii) stretched to maximum. (b) Working principle of the HFSSs; the states i, ii, and iii correspond to i, ii, and iii of (a). (c) Simulation results of the electric potential model using the COMSOL software. (d) V_{OC}, (e) I_{SC}, and (f) Q_{SC} of the HFSSs at a tensile strain of 1−80%.

stretching−releasing motions of HFSSs. During the stretching process, the helical structure elongated in the longitudinal direction, where the detachment occurred in adjacent nylon and PTFE until the maximum stretch strain. The nylon and PTFE get close to each other while the device is released. Figure 1b shows photographs of the HFSS under strains of 0% and 80%, respectively. The insets show the details of the HFSS before and after stretching.

The introduction of conductive electrodes is the key to the fabrication of the FS-TENG. In this work, we adopt a method widely used in textile engineering, namely, covered core−shell fibers. The fabrication process of the HFSSs is presented in Figure 1c. As displayed in Figure 1c-i and c-ii, the PTFE fibers or nylon fibers are used as shell fibers and the silver-plated fibers are selected as core fibers. The shell fibers are twined around the core fibers and interwoven with each other in the tightening sleeve to fabricate core−shell fibers through a multiaxial fiber winding machine (Figure S1, Supporting Information). The structure can be seen from the schematic diagram of the core−shell fiber (Figure 1c-iii and c-iv) and the cross-section of the core−shell fiber SEM image (Figure 1e). In addition, the core−shell fibers can be large-scale fabricated because the preparation process is continuous and mechanized. Figure 1c-v shows a photograph of two rolls of core−shell fibers fabricated by the winding machine. It is worth noting that the PTFE fibers can be pressed into a flat shape by an electric iron at 130 °C (Figure S2a, Supporting Information). SEM images in Figure 1f and g show the PTFE/Ag braided fiber based on untreated and treated PTFE, respectively. The V_{OC} of the PTFE/Ag braided fiber based on treated PTFE increased by about 50% under the same trigger conditions (Figure S2b and c, Supporting Information). This may be because the treated PTFE fibers can wrap the core fiber more tightly. In the end, the wrapping procedure is displayed in Figure 1c-vi. A pair of synchronously running motors drive the PTFE/Ag braided fibers and nylon/Ag braided fibers to alternately wind on the substrate fiber to form the HFSSs. It is worth noting that in order to keep two braided fibers in close contact during winding, the α and β angles (between braided fibers and substrate fibers) should be as consistent as possible (Figure 1c-vi). As exhibited in Figure S3 (Supporting Information), the HFSSs can withstand various complex mechanical deformations including twisting, knotting, and bending, which shows the good flexibility of the HFSSs.

The working principle of the HFSSs can be explained by coupling contact electrification and electrostatic induction, as illustrated in Figure 2a and b. At the initial state, two triboelectric materials (PTFE and nylon) are in contact. Because of the opposite triboelectric polarities of PTFE and nylon, the electrons are injected from nylon into PTFE, and the equivalent negative and positive triboelectric charges will be induced on their surfaces (Figure 2a-i and b-i). Once the HFSSs are stretched by external forces, the contacting surfaces of the nylon/Ag braided fiber and the PTFE/Ag braided fiber begin to separate. An electric potential difference will be built upon the two surfaces, which drives free electrons to flow from

https://doi.org/10.1021/acsnano.1c09792
ACS Nano XXXX, XXX, XXX−XXX

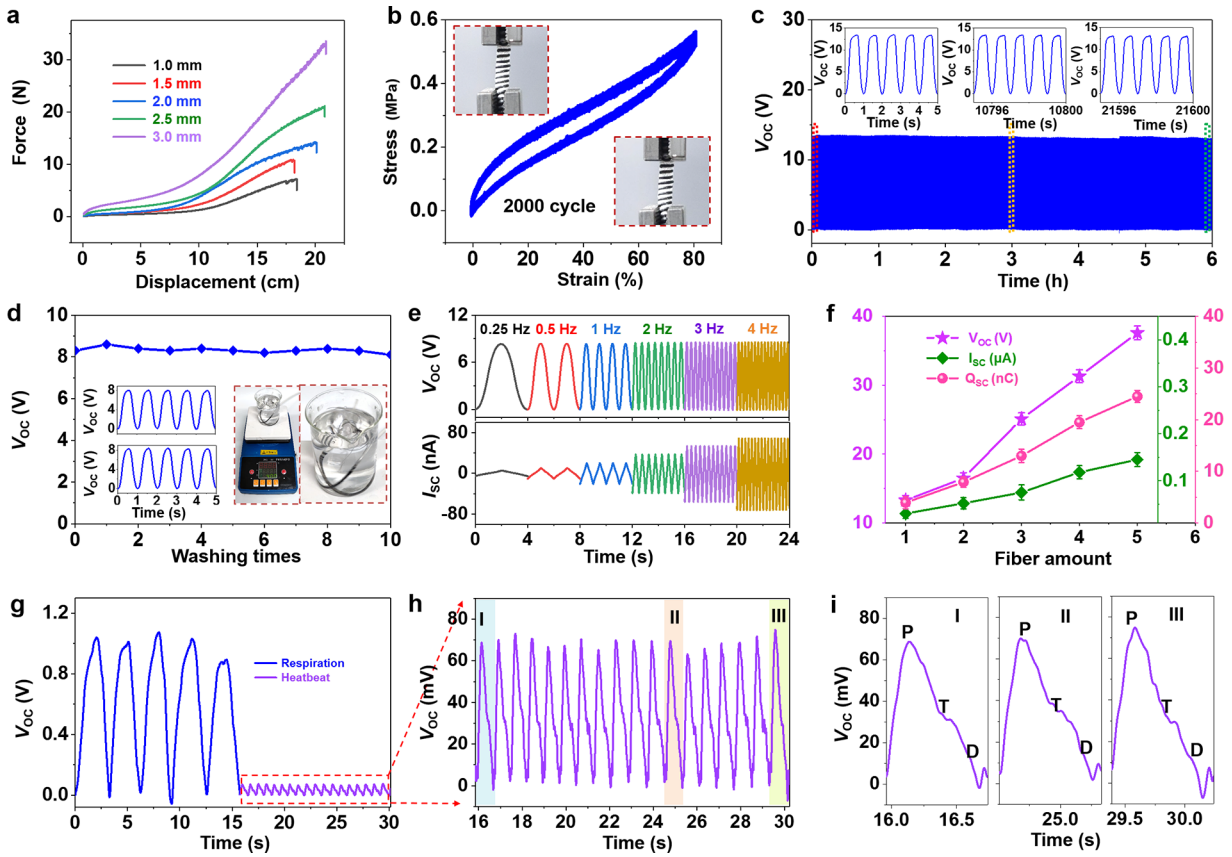

Figure 3. Mechanical properties and electrical output characteristics of the HFSSs. (a) Displacement−force curve of the stretchable substrate fiber with different diameters. (b) Stress−strain curve of the HFSSs being stretched and released for 2000 cycles. The insets are photos of the HFSS before and after the experiment, respectively. (c) Output stability and reliability of the HFSS. Insets are enlarged V_{OC} waveforms in the first, middle, and last five cycles, respectively. (d) Electrical output of the HFSS after 10 times washing. The inset photos are a simulated laundering environment, and the inset curves are the detailed V_{OC} curves of the unwashed and after 10 times washed HFSS, respectively. (e) V_{OC} and I_{SC} of the HFSS under different stretching frequencies (0.25−4 Hz). (f) Electrical output of different numbers of HFSSs (the original length is 10 cm, the elongation is 60%, and the stretching frequency is 1 Hz). (g) Signals of breathing (blue curve on the left) and heartbeat (purple curve on the right) collected using the chest straps. (h) Enlarged views of the output waveform of the heartbeat. (i) Magnified waveform extracted from (h), containing "P", "T", and "D" peaks.

the PTFE/Ag braided fiber to the nylon/Ag braided fiber (Figure 2a-ii and b-ii). When the HFSSs continue to be stretched, the gap between two surfaces increases, and the electric potential eventually reaches equilibrium (Figure 2a-iii and b-iii). When the external force is removed, the HFSSs return to their initial position, and the nylon/Ag braided fiber and PTFE/Ag braided fiber are brought into contact. In the process, free electrons flow from the nylon/Ag braided fiber to the PTFE/Ag braided fiber (Figure 2a-ii and b-iv). In the end, the HFSS returns to its original state, making a complete cycle of electricity generation. An electric potential model is simulated to further explain the principle of electricity generation by using COMSOL software (Figure 2c).

To quantitatively characterize the electrical output performance of the HFSSs, a test platform was constructed. As exhibited in Figure S4 (Supporting Information), a linear motor is utilized to provide the power for stretching motion. First of all, the effect of tensile strain on electrical output is investigated. An HFSS with a length of 10 cm is measured at a fixed stretching frequency of 1 Hz. As shown in Figure 2d−f, the open-circuit voltage (V_{OC}), short-circuit current (I_{SC}), and short-circuit charge transfer (Q_{SC}) increase with the increment of stretching strain (1−80%) due to the more sufficient contact and separation between the two braided fibers at larger stretching strain. There are two stages with the increase of stretching strain. In the first stage, the electrical output rises rapidly when the stretch strain increases from 0% to 50%, while the second stage (50−80%) has a lower change rate. It is worth noting that the HFSSs can still have a stable electrical output of 0.5 V with the stretch strain of 1%, which shows that the HFSSs are sensitive to stretch strain. Moreover, as depicted in Figure S5 (Supporting Information), the HFSSs exhibit an immediate response time of 70 ms and a recovery time of 71 ms under 5 Hz stretching frequency.

The resilience of HFSSs is mainly derived from stretchable substrate fibers. However, excessive elasticity will hinder the stretching of the HFSSs. On the contrary, if the elastic force is too small, the HFSSs cannot recover quickly. The stretchability of the substrate fibers with different diameters is tested. Figure 3a exhibits displacement−force curves. As we can see, the elongation rate of the substrate fibers is more than 400%, which is sufficient to make HFSSs. The resilience increases with the increasing diameter. Therefore, we can select stretchable substrate fibers with different diameters according to different application scenarios. In this work, a stretchable substrate fiber with a diameter of 1.5 mm is chosen to fabricate the HFSSs. In addition, a cyclic tensile test is executed for the HFSS sample (the original length of 9 mm, 80% tensile strain).

https://doi.org/10.1021/acsnano.1c09792
ACS Nano XXXX, XXX, XXX−XXX

As shown in Figure 3b, the mechanical behavior and the helical structure of the HFSS have no obvious change after being stretched and released for 2000 cycles. The insets display the photos of the HFSS before and after the cyclic tensile test. It can be seen that the HFSSs have good tensile properties.

The stability and reliability of electrical output are indispensable for practical applications. To evaluate them, an HFSS with a length of 10 cm is continuously stretched and released under a stretch strain of 60% at 1 Hz stretching frequency for over 6 h. The corresponding V_{OC} is shown in Figure 3c. During the more than 20 000 stretching cycles, the V_{OC} exhibits no obvious deterioration, which indicates that the HFSSs have high stability and good durability. For a detailed comparison, the enlarged V_{OC} waveforms in the first, middle, and last five stretching cycles are exhibited in the insets of Figure 3c. Moreover, machine washability is also an important performance indicator for wearable devices. To demonstrate the washability of the HFSSs, a simulated domestic laundering environment is cultivated (insets of Figure 3d). The electrical output of the HFSSs is tested after being washed different times. As displayed in Figure 3d, the electrical output of the HFSSs shows no significant degradation after 10 times washing (stirring rate is 400 rpm, each washing time is 30 min). The insets exhibit the detailed V_{OC} curve of the unwashed and after 10 times washed HFSS, respectively.

The V_{OC}, I_{SC}, and Q_{SC} are measured when the stretching frequency increases from 0.25 Hz to 4 Hz (original length: 10 cm, stretch strain: 40%). It can be seen from Figures 3e and S6 (Supporting Information) that the V_{OC} and Q_{SC} remain constant, while the I_{SC} gradually increases from 2 nA to 68 nA. Furthermore, environmental conditions can also influence the output of the HFSS, such as temperature and humidity. As presented in Figure S7 (Supporting Information), the V_{OC} increases from 8.5 V to 10.4 V when the temperature rises from 10 °C to 45 °C. And the trend of the I_{SC} is similar to the V_{OC}; it also increases from 15 nA to 25 nA. Figure S8 (Supporting Information) is the V_{OC} and I_{SC} of the HFSS for different relative humidity values (6−76%). It can be seen that both the V_{OC} and the I_{SC} of the HFSS decrease with the increase of relative humidity. The V_{OC} and the I_{SC} drop by 20% and 19%, respectively. The output power density is investigated by $W = U^2/R$, where U is the output voltage and R is the applied external resistance. The relationships between power density and resistance are exhibited in Figure S9 (Supporting Information). Both the output voltage and the power density present a trend of initial stability and then a rapid increase with the increase of external load resistance. The maximum peak output power density is 4.3 μW/m when the external load resistance is about 250 MΩ. To investigate the charging ability, an HFSS is used to charge capacitance of different capacities (0.1−22 μF) under the testing conditions of fixed strains (40%) and stretching frequency (1 Hz). As exhibited in Figure S10 (Supporting Information), it can be observed that the electricity generated from the HFSSs can be stored in the capacitance. In addition, the output of a single HFSS is limited. Therefore, it is necessary to verify that the electrical output can be enhanced by connecting multiple HFSSs in parallel. The electrical output of different numbers of HFSSs is measured, and the test results are illustrated in Figure 3f (the original length is 10 cm, the elongation is 60%, and the stretching frequency is 1 Hz). Figure S11a−c (Supporting Information) further shows the V_{OC}, I_{SC}, and Q_{SC} of the HFSSs under strains of 15%, 30%, 45%, 60%, and 80%, with the number of HFSSs being 1, 2, 3, 4, and 5, respectively. To understand the changing trend of electrical output more clearly, in Figure S11d−f (Supporting Information), the peak values of V_{OC}, I_{SC}, and Q_{SC} of the HFSSs under different strains from Figure S9a−c are extracted. It can be seen clearly that all the electrical output increases with the applied strains and the number of fibers. The output under five HFSSs with 80% strain can reach ∼40 V, ∼0.16 μA, and ∼26 nC, respectively. This shows that the output can be effectively increased by increasing the number of HFSSs, which is extremely important for practical applications. The detailed electrical output curves are displayed in Figures S12−14 (Supporting Information).

The HFSSs are capable of capturing the detailed physiological signals of breathing and heartbeat. Here, we stitch the HFSSs into a chest strap and fasten it to the chest to monitor the breathing and heartbeat signals. Figure 3g shows the electrical signals of breathing and heartbeat collected with a chest strap. On the left side of the figure are the electrical signals showing that respiration and heartbeat work together. On the right side of the figure is the heartbeat signals when the human is holding its breath. Figure 3h exhibits the enlarged views of the output waveform. It can be observed that the HFSSs can steadily produce a responding output waveform following the heartbeat, indicating a frequency of 74 beats/min. Three measured waveforms are extracted, as illustrated in Figure 3i. They have three characteristic peaks, "P" (percussion), "T" (tidal), and "D" (diastolic), which are the essential information for monitoring the pulse. In addition, an HFSS is attached to the finger or knee to monitor the bending angles. As displayed in Figure S15a and b (Supporting Information), the V_{OC} of the HFSS is linearly proportional to the bending angles of the joint because the elongation of the HFSS increases with the increase of the joint bending angle. Figure S16 (Supporting Information) shows the knee bent at different angles according to the scale placed on the ground. Built on the relationship between the bending angles and the V_{OC}, the bending angle can be judged by the V_{OC}. The power twister is used to further verify it. As exhibited in Figure S17a (Supporting Information), an HFSS is fixed to the power twister and stretched as the power twister bends. The V_{OC} increases from 1.5 to 20 V with the increase in bending angles, and there is just one corresponding V_{OC} value for a bending angle (Figure S17b, Supporting Information). This result is further verified by repeating the bending experiment five times (Figure S17c, Supporting Information). It can be seen that there is a stable and repeatable relationship between the bending angle and the V_{OC} of the HFSSs, which fits the piecewise linear relationship (Figure S17d, Supporting Information). Here, based on this linear relationship, a real-time and self-powered angle-sensing system is developed and implemented by using the LabVIEW software, which can not only judge the bending angles of the power twister but also accurately record the number of bendings, as illustrated in Figure S17e and Movie S1 (Supporting Information). The HFSSs are going to be used as angle sensors, which have potential applications in robotics and human activity monitoring.

Respiratory information such as FVC, FEV1, and PEF is very important for assessment of respiratory condition, diagnosis of disease, and medical treatment. "FVC" refers to the maximum volume of air that can be exhaled as soon as possible after inhaling as much as possible, and "FEV1" is the amount of air that is exhaled within the first second. The value

https://doi.org/10.1021/acsnano.1c09792
ACS Nano XXXX, XXX, XXX−XXX

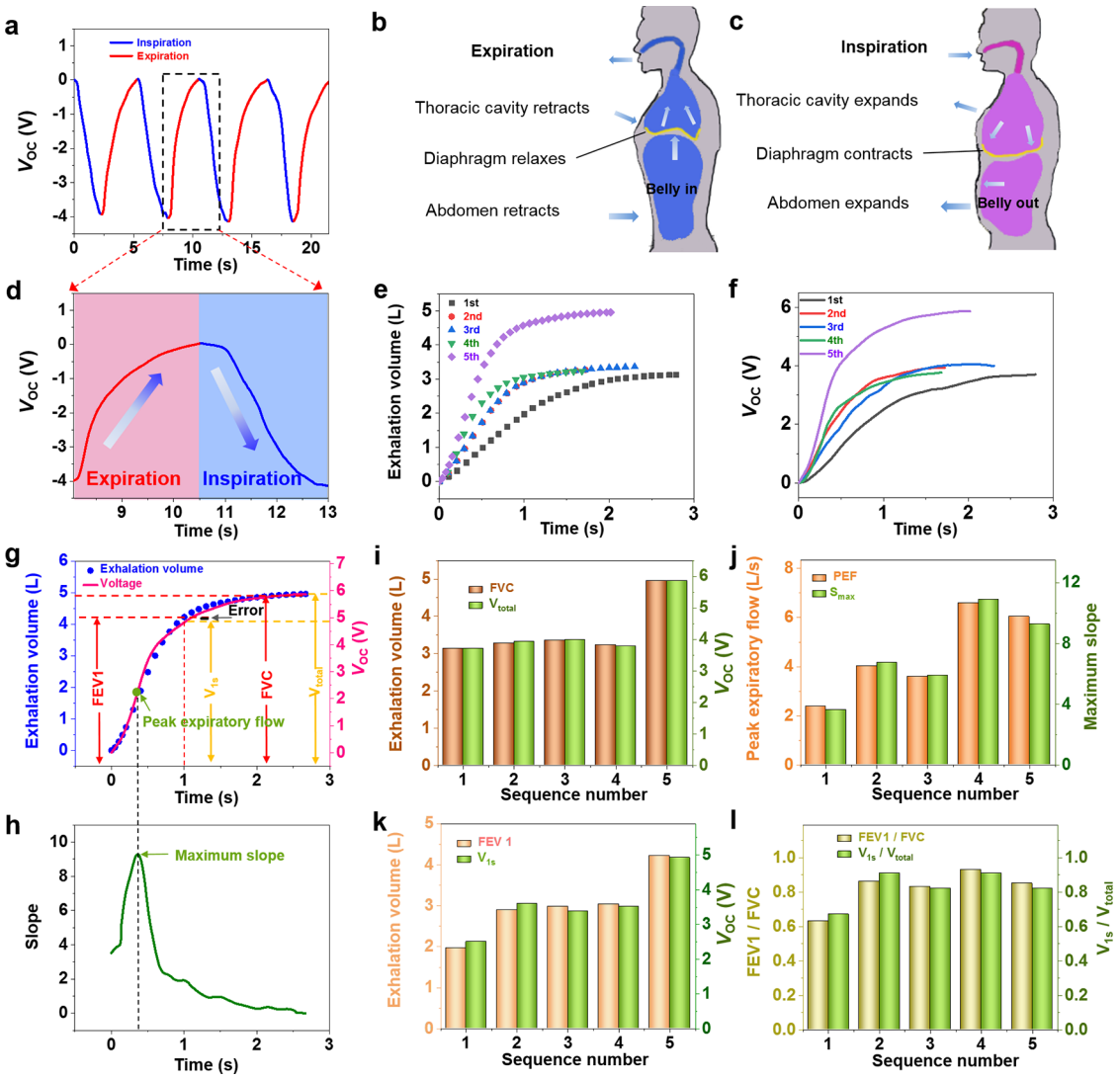

Figure 4. HFSSs are used to measure FVC, FEV1, and PEF. (a) Regular electrical signals of the HFSS-based chest strap as the human body breathes. (b, c) Schematic diagram of the expansion/contraction of the chest and abdomen as the human body breathes. (d) Electrical signal corresponding to a complete respiratory cycle. (e) Curves of the volume of exhaled air over time measured by a commercial spirometer. (f) V_{OC} curves of the HFSSs with time. (g) Corresponding relationship between V_{OC} curves and volume of exhaled air curves over time. (h) Slope calculated from the $v-t$ curve in (g). Comparison of the measurement results of the two measurement methods (i) FVC and V_{total}; (j) PEF and Smax; (k) FEV 1 and V_{1s}; and (l) FEV1/FVC and V_{1s}/V_{total}.

of FEV1/FVC is an essential basis for judging whether there is a respiratory disease.[39,40] Monitoring the breathing by wearable sensors is particularly attractive because it is convenient, comfortable, and nonintrusive. Here, the HFSS-based chest strap is developed and subsequently secured at the upper part of the abdomen for monitoring human breathing. It is worth noting that data acquisition and processing for detecting respiratory disease are prominent. In order to get rid of environmental noise, the signals are filtered according to the rate of respiration (the adult respiratory rate is about 16−20 breaths per min). As illustrated in Figure 4b and c, on inhalation, the diaphragm contracts and pulls down to increase the volume of the thoracic cavity and abdomen, which stretches the HFSSs and gives an electrical signal. On the contrary, the diaphragm relaxes to reduce the volume of the thoracic cavity and abdomen during expiration, which releases the HFSSs and gives an opposite electrical signal. In the process, HFSSs are regularly stretched and contracted, which generates continuous electrical signals (Figure 4a). Figure 4d is an electrical signal corresponding to a complete respiratory cycle.

Inspiratory/expiratory volumes refer to the amount of inhaled or exhaled air in one breathing cycle. The exhalation process of the human body is measured simultaneously by both a commercial electronic spirometer (Figure S18, Supporting Information) and an HFSS-based chest strap fastened on the upper part of the abdomen. Figure 4e shows the curves of the volume of exhaled air over time measured by a commercial electronic spirometer, and Figure 4f shows the V_{OC} curves of the HFSSs. It can be seen that the trend of the five pairs of curves displays a good match over the entire time domain (the sequence number represents the order of tests). This good match could be attributed to the high sensitivity of the HFSSs to stretching. Figure S19 (Supporting Information) is a detailed comparison of results measured by two test methods. The relation between the V_{OC} of HFSSs and the volume of exhaled air is illustrated in Figure 4g. The difference between positive and negative peaks is indicated as V_{total}, which

https://doi.org/10.1021/acsnano.1c09792
ACS Nano XXXX, XXX, XXX−XXX

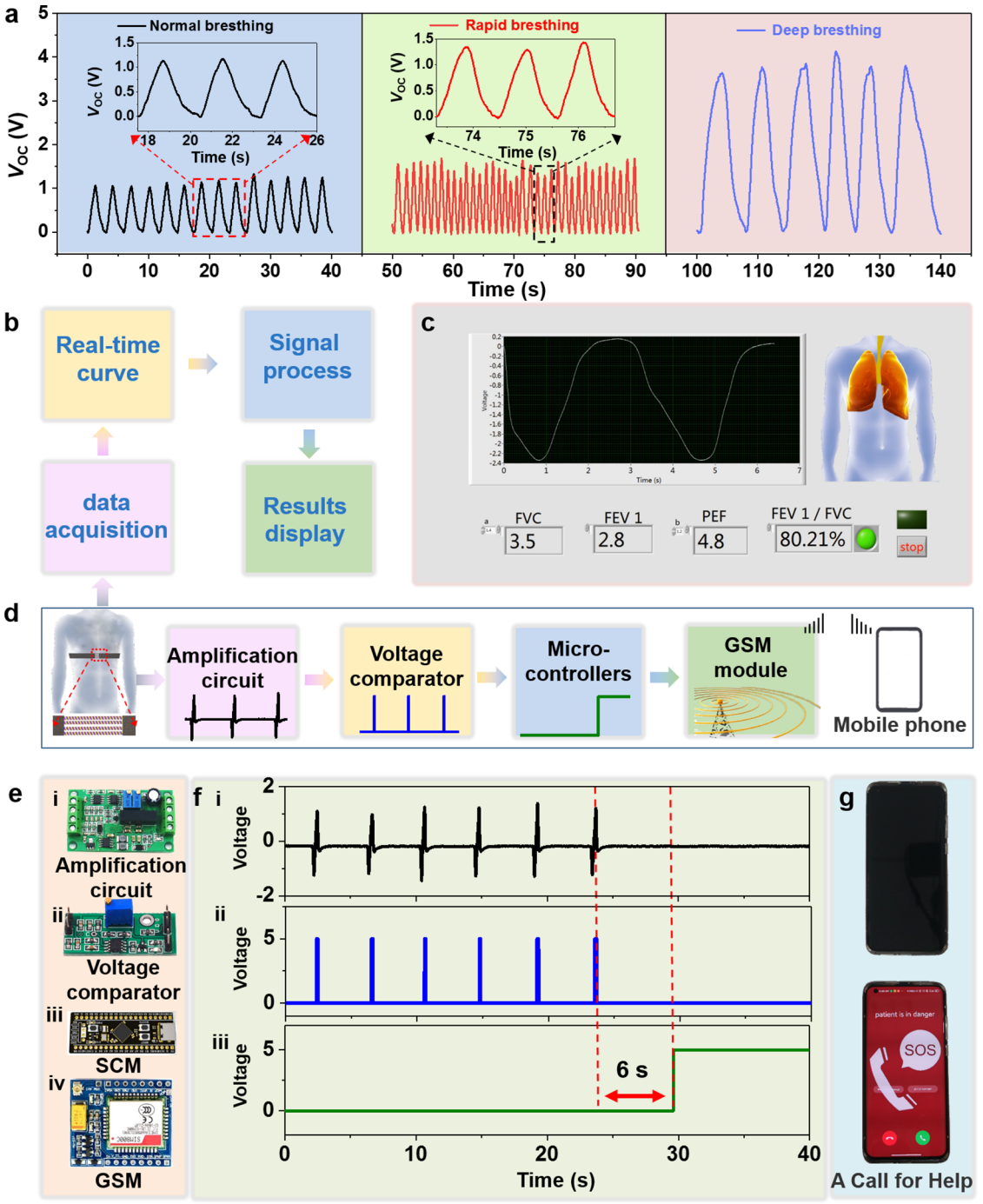

Figure 5. Application demonstration of respiratory monitoring. (a) Voltage signals recorded normal, rapid, and deep breathing states; the insets show the enlarged curves. (b) Schematic diagram of the HFSS-based self-powered smart spirometer system. (c) Demonstration of the self-powered smart spirometer system and display of real-time measuring result. (d) Schematic diagram of a real-time respiratory monitoring and intelligent alert system. (e) Circuit boards for signal conditioning and transmitting. (f) (i) Breathing signals after being filtered and amplified. (ii) Square signal switched by the relay. (iii) Operating voltage of the GSM module switches between high and low potentials. (g) A mobile telephone is called when a patient stops breathing for more than 6 s.

positively correlates with the FVC, and the FEV1 corresponds to the difference between the value in the first second and the negative peaks (V_{1s}). The rate of exhalation corresponds to the slope of the V–t curve (Figure 4h), and the PEF corresponds to the maximum slope (S_{max}). Here, the FVC, FEV1, and PEF can be measured directly by a commercial electronic spirometer. As displayed in Figure 4i–l, the five measurements of FVC, FEV1, PEF, and FEV1/FVC are compared with the corresponding V_{OC}, respectively. It can be seen that there is a small error between the results measured by the two methods. Therefore, the HFSSs can be used to assess respiration.

In addition to quantifying the volume of airflow of each expiration, the HFSSs can also be employed to monitor human breathing continuously. As illustrated in Figure 5a, the electrical signals of the HFSSs record three different respiratory patterns, namely, normal, rapid, and deep breath-

https://doi.org/10.1021/acsnano.1c09792
ACS Nano XXXX, XXX, XXX–XXX

ing. It can be clearly seen that there are obvious differences in respiratory intensity and rate under different respiratory patterns. For example, rapid breathing generates more V_{OC} peaks than normal breathing in the same amount of time. It can be obtained from the number of V_{OC} peaks that the respiration rate of normal breathing is about 20 breaths/min, while for hurried breathing, it can reach 54 breaths/min. In addition, the V_{OC} becomes larger and the peak width becomes wider when the human body breathes deeply. Compared to normal breathing, deep breathing has a higher intensity but a lower rate.

Based on the good match between the V_{OC} of the HFSSs and the commercial electronic spirometer measurement results, a self-powered smart spirometer has been developed, which can quantify the volume of airflow per expiration. As shown in Figure 5b, an HFSS-based chest strap is secured to the upper part of the abdomen to convert the expansion and contraction of the abdomen into electrical signals. Then the results are obtained by analyzing the amplitude and slope of the waveforms. Figure 5c and Movie S2 (Supporting Information) show the self-powered smart spirometer, including real-time voltage signals, calculation results of FVC, FEV1, PEF, and FEV1/FVC, and final diagnosis results. Among them, FEV1/FVC is an important indicator to judge whether there is a respiratory disease.[39,40] Here, the standard of the FEV1/FVC is set at 80%. When the measurement value is greater than this value, the spirometer's indicator shows green, indicating normal; otherwise, the indicator shows red, indicating possible disease. It is worth noting that "a" and "b" are variable parameters in the formulas FVC = aV_{total}, FEV1 = aV_{1s}, and PEF = bS_{max}. The changeable parameters change with the change of the test object, so they need to be corrected for different test subjects.

In addition, respiratory arrest is often life-threatening because it is not found in time. Therefore, a self-powered intelligent alarm based on HFSSs is developed. As displayed in Figure 5d, the alarm consists of an HFSS-based chest strap, a signal processing circuit, a global system for a mobile communication (GSM) module, and a mobile phone. HFSS-based chest straps can continuously monitor the respiratory status of the human body in real time. As displayed in Figure S20 (Supporting Information), a chest strap is attached to the chest or abdomen to monitor chest breathing and abdominal breathing. It can be seen that the HFSSs can provide a steady electrical output in both sitting and lying positions, respectively. The signal-processing circuit includes an amplification circuit (Figure 5e-i) to amplify the electrical signals and eliminate some of the interference, a voltage comparator (Figure 5e-ii) to convert the amplified signals into stable square wave signals, and a single-chip microcomputer (SCM, Figure 5e-iii) to receive the square wave signals and send instructions to the GSM (Figure 5e-iv). As displayed in Figure 5f, the top is the amplified signal produced by the HFSSs, and the middle is the square wave signal transmitted by the voltage comparator. The bottom is the switch signal of the SCM, which is utilized to control the GSM. When the body normally breathes, the HFSSs produce continuous electrical signals. Once the respiration stops, the electrical signal is discontinued. When the signal stops for more than 6 s, the GSM module will automatically call the preset mobile phone for help under the control of the SCM (Figure 5g and Movie S3, Supporting Information), so that the patient can be treated as soon as possible.

CONCLUSION

In this work, wearable and self-powered strain sensors are constructed by introducing helical structure braided fibers on a stretchable substrate fiber. Owing to the structure, the HFSSs show high sensitivity to strain, and a single HFSS (with a length of 10 cm) can output 0.5 V even under 1% stretch strain. The HFSSs can sense the contraction and relaxation of the thoracic cavity and abdomen caused by the heartbeat and breathing. Based on the HFSSs, a wearable self-powered real-time respiratory monitoring system is developed. The smart spirometer can be utilized to diagnose potential respiratory diseases by measuring FVC, FEV1, and PEF. The self-powered intelligent alarm can distinguish different respiratory patterns and call the preset mobile phone for help when the patients stop breathing for more than 6 s. This work designs a type of FS-TENGs with high sensitivity to strain, which can be used for real-time respiratory monitoring.

EXPERIMENTAL SECTION

Fabrication of HFSSs. The nylon/Ag braided fibers and PTFE/Ag braided fibers are core−shell fibers. The shell fibers (PTFE fiber or nylon fiber) were twined around the core fiber (silver-plated fiber) and interwoven with each other by a multiaxial fiber winding machine. Then, two identical motors were placed opposite each other, and the two ends of the stretchable substrate fiber were fixed on the motors. In the end, a pair of synchronously running motors drove the nylon/Ag braided fibers and PTFE/Ag braided fibers to alternately wind on the substrate fiber to form the final fiber.

Characterization and Measurement. The electrical output performance was measured using a Keithley 6514 electrometer with a Labview program. A linear mechanical motor provided the external forces for HFSSs to stretch and release. Field-emission scanning electron microscopy (FEI Nova Nano SEM 450) was utilized to observe the surface morphology and the section of fibers. A tensile machine (Instron EP3000) was utilized to test the cyclic tensile strength of HFSSs.

Self-Powered Smart Spirometer. An HFSS-based chest strap was used to convert the expansion and contraction of the human chest cavity and abdomen into electrical signals. The data processing and analysis software was constructed by a computer with LabVIEW. The software displays the measurement results, including real-time voltage signals, FVC, FEV1, PEF, and FEV1/FVC, and final diagnosis results. When the measurement value of FEV1/FVC is greater than 80%, the spirometer's indicator shows green, indicating normal; otherwise, the indicator shows red, indicating possible disease.

Self-Powered Intelligent Alarm. The HFSS-based chest strap continuously outputs electrical signals when the human body is breathing normally. Once breathing stops for more than 6 s, the SCM senses this and turns on the GSM module to call the corresponding mobile phone. The modules used include an amplification circuit (AD620), voltage comparator (LM393), SCM (STM 32F4), and GSM (SIM800C).

Informed consent was obtained from the volunteers who participated in the experiments.

ASSOCIATED CONTENT

Supporting Information

The Supporting Information is available free of charge at https://pubs.acs.org/doi/10.1021/acsnano.1c09792.

Figures S1−20: photos of multiaxial fiber winding machine; schematic diagram of the PTFE fiber treatment process; photographs of the HFSSs under different mechanical forces; schematic diagram of the test platform; response time of the HFSS at different stretching frequencies; Q_{SC} of the HFSS under different

https://doi.org/10.1021/acsnano.1c09792
ACS Nano XXXX, XXX, XXX−XXX

stretching frequencies; V_{OC} and I_{SC} of the HFSS at different temperatures and relative humidity; power density on the different external load resistances; charging curves of different capacitance capacities by a single HFSS; V_{OC}, I_{SC}, and Q_{SC} of different numbers of HFSSs under different strains; application of HFSSs as angle sensors; photos of commercial electronic spirometer; detailed comparison of results measured by the two test methods; output of abdominal breathing and chest breathing in sitting and lying positions (PDF)

Video 1: Bending angle monitoring of power twister (AVI)

Video 2: Respiratory parameters measured by HFSSs (AVI)

Video 3: System for breathing monitoring and calling for help (AVI)

AUTHOR INFORMATION

Corresponding Authors

Kai Dong − *CAS Center for Excellence in Nanoscience, Beijing Key Laboratory of Micro-Nano Energy and Sensor, Beijing Institute of Nanoenergy and Nanosystems, Chinese Academy of Sciences, Beijing 101400, People's Republic of China; School of Nanoscience and Technology, University of Chinese Academy of Sciences, Beijing 100049, People's Republic of China;* orcid.org/0000-0001-6314-1546; Email: dongkai@binn.cas.cn

Zhong Lin Wang − *CAS Center for Excellence in Nanoscience, Beijing Key Laboratory of Micro-Nano Energy and Sensor, Beijing Institute of Nanoenergy and Nanosystems, Chinese Academy of Sciences, Beijing 101400, People's Republic of China; School of Nanoscience and Technology, University of Chinese Academy of Sciences, Beijing 100049, People's Republic of China; CUSTech Institute of Technology, Wenzhou, Zhejiang 325024, People's Republic of China; School of Material Science and Engineering, Georgia Institute of Technology, Atlanta, Georgia 30332, United States;* orcid.org/0000-0002-5530-0380; Email: zlwang@gatech.edu

Authors

Chuan Ning − *CAS Center for Excellence in Nanoscience, Beijing Key Laboratory of Micro-Nano Energy and Sensor, Beijing Institute of Nanoenergy and Nanosystems, Chinese Academy of Sciences, Beijing 101400, People's Republic of China; School of Nanoscience and Technology, University of Chinese Academy of Sciences, Beijing 100049, People's Republic of China*

Renwei Cheng − *CAS Center for Excellence in Nanoscience, Beijing Key Laboratory of Micro-Nano Energy and Sensor, Beijing Institute of Nanoenergy and Nanosystems, Chinese Academy of Sciences, Beijing 101400, People's Republic of China; School of Nanoscience and Technology, University of Chinese Academy of Sciences, Beijing 100049, People's Republic of China*

Yang Jiang − *CAS Center for Excellence in Nanoscience, Beijing Key Laboratory of Micro-Nano Energy and Sensor, Beijing Institute of Nanoenergy and Nanosystems, Chinese Academy of Sciences, Beijing 101400, People's Republic of China; School of Nanoscience and Technology, University of Chinese Academy of Sciences, Beijing 100049, People's Republic of China*

Feifan Sheng − *CAS Center for Excellence in Nanoscience, Beijing Key Laboratory of Micro-Nano Energy and Sensor, Beijing Institute of Nanoenergy and Nanosystems, Chinese Academy of Sciences, Beijing 101400, People's Republic of China; Center on Nanoenergy Research, School of Physical Science and Technology, Guangxi University, Nanning 530004, People's Republic of China*

Jia Yi − *CAS Center for Excellence in Nanoscience, Beijing Key Laboratory of Micro-Nano Energy and Sensor, Beijing Institute of Nanoenergy and Nanosystems, Chinese Academy of Sciences, Beijing 101400, People's Republic of China; Center on Nanoenergy Research, School of Physical Science and Technology, Guangxi University, Nanning 530004, People's Republic of China*

Shen Shen − *CAS Center for Excellence in Nanoscience, Beijing Key Laboratory of Micro-Nano Energy and Sensor, Beijing Institute of Nanoenergy and Nanosystems, Chinese Academy of Sciences, Beijing 101400, People's Republic of China*

Yihan Zhang − *CAS Center for Excellence in Nanoscience, Beijing Key Laboratory of Micro-Nano Energy and Sensor, Beijing Institute of Nanoenergy and Nanosystems, Chinese Academy of Sciences, Beijing 101400, People's Republic of China; School of Nanoscience and Technology, University of Chinese Academy of Sciences, Beijing 100049, People's Republic of China*

Xiao Peng − *CAS Center for Excellence in Nanoscience, Beijing Key Laboratory of Micro-Nano Energy and Sensor, Beijing Institute of Nanoenergy and Nanosystems, Chinese Academy of Sciences, Beijing 101400, People's Republic of China; School of Nanoscience and Technology, University of Chinese Academy of Sciences, Beijing 100049, People's Republic of China*

Complete contact information is available at: https://pubs.acs.org/10.1021/acsnano.1c09792

Author Contributions

#C.N., R.C., and Y.J. contributed equally to this work.

Notes

The authors declare no competing financial interest.

ACKNOWLEDGMENTS

The authors are grateful for the support received from National Natural Science Foundation of China (Grant No. 22109012), Natural Science Foundation of the Beijing Municipality (Grant No. 2212052), and the Fundamental Research Funds for the Central Universities (Grant No. E1E46805).

REFERENCES

(1) Trung, T. Q.; Lee, N. E. Flexible and Stretchable Physical Sensor Integrated Platforms for Wearable Human-Activity Monitoringand Personal Healthcare. *Adv. Mater.* **2016**, *28*, 4338−4372.

(2) Shen, S.; Xiao, X.; Xiao, X.; Chen, J. Wearable triboelectric nanogenerators for heart rate monitoring. *Chem. Commun. (Camb.)* **2021**, *57*, 5871−5879.

(3) Ma, Y.; Zheng, Q.; Liu, Y.; Shi, B.; Xue, X.; Ji, W.; Liu, Z.; Jin, Y.; Zou, Y.; An, Z.; Zhang, W.; Wang, X.; Jiang, W.; Xu, Z.; Wang, Z. L.; Li, Z.; Zhang, H. Self-Powered, One-Stop, and Multifunctional Implantable Triboelectric Active Sensor for Real-Time Biomedical Monitoring. *Nano Lett.* **2016**, *16*, 6042−6051.

(4) Imani, S.; Bandodkar, A. J.; Mohan, A. M.; Kumar, R.; Yu, S.; Wang, J.; Mercier, P. P. A wearable chemical-electrophysiological

https://doi.org/10.1021/acsnano.1c09792
ACS Nano XXXX, XXX, XXX−XXX

hybrid biosensing system for real-time health and fitness monitoring. *Nat. Commun.* **2016**, *7*, 11650.
(5) Wang, M.; Zhang, J.; Tang, Y.; Li, J.; Zhang, B.; Liang, E.; Mao, Y.; Wang, X. Air-Flow-Driven Triboelectric Nanogenerators for Self-Powered Real-Time Respiratory Monitoring. *ACS Nano* **2018**, *12*, 6156−6162.
(6) Peng, X.; Dong, K.; Ning, C.; Cheng, R.; Yi, J.; Zhang, Y.; Sheng, F.; Wu, Z.; Wang, Z. L. All-Nanofiber Self-Powered Skin-Interfaced Real-Time Respiratory Monitoring System for Obstructive Sleep Apnea-Hypopnea Syndrome Diagnosing. *Adv. Funct. Mater.* **2021**, *31*, 2103559.
(7) Su, Y.; Chen, G.; Chen, C.; Gong, Q.; Xie, G.; Yao, M.; Tai, H.; Jiang, Y.; Chen, J. Self-Powered Respiration Monitoring Enabled By a Triboelectric Nanogenerator. *Adv. Mater.* **2021**, *33*, 2101262.
(8) Liu, Z.; Zhao, Z.; Zeng, X.; Fu, X.; Hu, Y. Expandable microsphere-based triboelectric nanogenerators as ultrasensitive pressure sensors for respiratory and pulse monitoring. *Nano Energy* **2019**, *59*, 295−301.
(9) Zhao, Z.; Yan, C.; Liu, Z.; Fu, X.; Peng, L. M.; Hu, Y.; Zheng, Z. Machine-Washable Textile Triboelectric Nanogenerators for Effective Human Respiratory Monitoring through Loom Weaving of Metallic Yarns. *Adv. Mater.* **2016**, *28*, 10267−10274.
(10) Dinh, T.; Nguyen, T.; Phan, H. P.; Nguyen, N. T.; Dao, D. V.; Bell, J. Stretchable respiration sensors: Advanced designs and multifunctional platforms for wearable physiological monitoring. *Biosens Bioelectron* **2020**, *166*, 112460.
(11) Liu, Y.; Zhao, L.; Avila, R.; Yiu, C.; Wong, T.; Chan, Y.; Yao, K.; Li, D.; Zhang, Y.; Li, W.; Xie, Z.; Yu, X. Epidermal electronics for respiration monitoring via thermo-sensitive measuring. *Mater. Today Phys.* **2020**, *13*, 100199.
(12) Zhang, B.; Tang, Y.; Dai, R.; Wang, H.; Sun, X.; Qin, C.; Pan, Z.; Liang, E.; Mao, Y. Breath-based human−machine interaction system using triboelectric nanogenerator. *Nano Energy* **2019**, *64*, 103953.
(13) Fan, F. R.; Lin, L.; Zhu, G.; Wu, W.; Zhang, R.; Wang, Z. L. Transparent triboelectric nanogenerators and self-powered pressure sensors based on micropatterned plastic films. *Nano Lett.* **2012**, *12*, 3109−14.
(14) Dong, K.; Wang, Z. L. Self-charging power textiles integrating energy harvesting triboelectric nanogenerators with energy storage batteries/supercapacitors. *J. Semicond.* **2017**, *38*, 105009.
(15) Fan, F.-R.; Tian, Z.-Q.; Lin Wang, Z. Flexible triboelectric generator. *Nano Energy* **2012**, *1*, 328−334.
(16) Wang, Z. L. On Maxwell's displacement current for energy and sensors: the origin of nanogenerators. *Mater. Today* **2017**, *20*, 74−82.
(17) Wang, Z. L. On the first principle theory of nanogenerators from Maxwell's equations. *Nano Energy* **2020**, *68*, 104272.
(18) Peng, X.; Dong, K.; Wu, Z.; Wang, J.; Wang, Z. L. A review on emerging biodegradable polymers for environmentally benign transient electronic skins. *J. Mater. Sci.* **2021**, *56*, 16765−16789.
(19) Wang, H.; Zhang, Y.; Liang, X.; Zhang, Y. Smart Fibers and Textiles for Personal Health Management. *ACS Nano* **2021**, *15*, 12497−12508.
(20) Peng, X.; Dong, K.; Ye, C.; Jiang, Y.; Zhai, S.; Cheng, R.; Liu, D.; Gao, X.; Wang, J.; Wang, Z. L. A breathable, biodegradable, antibacterial, and self-powered electronic skin based on all-nanofiber triboelectric nanogenerators. *Sci. Adv.* **2020**, *6*, No. eaba9624.
(21) Dong, K.; Peng, X.; Wang, Z. L. Fiber/Fabric-Based Piezoelectric and Triboelectric Nanogenerators for Flexible/Stretchable and Wearable Electronics and Artificial Intelligence. *Adv. Mater.* **2020**, *32*, 1902549.
(22) Ning, C.; Dong, K.; Cheng, R.; Yi, J.; Ye, C.; Peng, X.; Sheng, F.; Jiang, Y.; Wang, Z. L. Flexible and Stretchable Fiber-Shaped Triboelectric Nanogenerators for Biomechanical Monitoring and Human-Interactive Sensing. *Adv. Funct. Mater.* **2021**, *31*, 2006679.
(23) Zhu, C.; Li, R.; Chen, X.; Chalmers, E.; Liu, X.; Wang, Y.; Xu, B. B.; Liu, X. Ultraelastic Yarns from Curcumin-Assisted ELD toward Wearable Human−Machine Interface Textiles. *Adv. Sci.* **2020**, *7*, 2002009.
(24) Guan, X.; Xu, B.; Wu, M.; Jing, T.; Yang, Y.; Gao, Y. Breathable, washable and wearable woven-structured triboelectric nanogenerators utilizing electrospun nanofibers for biomechanical energy harvesting and self-powered sensing. *Nano Energy* **2021**, *80*, 105549.
(25) Kwak, S. S.; Kim, H.; Seung, W.; Kim, J.; Hinchet, R.; Kim, S. W. Fully Stretchable Textile Triboelectric Nanogenerator with Knitted Fabric Structures. *ACS Nano* **2017**, *11*, 10733−10741.
(26) Ning, C.; Tian, L.; Zhao, X.; Xiang, S.; Tang, Y.; Liang, E.; Mao, Y. Washable textile-structured single-electrode triboelectric nanogenerator for self-powered wearable electronics. *J. Mater. Chem. A* **2018**, *6*, 19143−19150.
(27) Dong, K.; Peng, X.; An, J.; Wang, A. C.; Luo, J.; Sun, B.; Wang, J.; Wang, Z. L. Shape adaptable and highly resilient 3D braided triboelectric nanogenerators as e-textiles for power and sensing. *Nat. Commun.* **2020**, *11*, 2868.
(28) Yu, A.; Pu, X.; Wen, R.; Liu, M.; Zhou, T.; Zhang, K.; Zhang, Y.; Zhai, J.; Hu, W.; Wang, Z. L. Core-Shell-Yarn-Based Triboelectric Nanogenerator Textiles as Power Cloths. *ACS Nano* **2017**, *11*, 12764−12771.
(29) Leber, A.; Dong, C.; Chandran, R.; Das Gupta, T.; Bartolomei, N.; Sorin, F. Soft and stretchable liquid metal transmission lines as distributed probes of multimodal deformations. *Nat. Electron.* **2020**, *3*, 316−326.
(30) Fan, W.; He, Q.; Meng, K.; Tan, X.; Zhou, Z.; Zhang, G.; Yang, J.; Wang, Z. L. Machine-knitted washable sensor array textile for precise epidermal physiological signal monitoring. *Sci. Adv.* **2020**, *6*, No. eaay2840.
(31) Ning, C.; Dong, K.; Gao, W.; Sheng, F.; Cheng, R.; Jiang, Y.; Yi, J.; Ye, C.; Peng, X.; Wang, Z. Dual-mode Thermal-Regulating and Self-Powered Pressure Sensing Hybrid Smart Fibers. *Chem. Eng. J.* **2021**, *420*, 129650.
(32) Zhang, D.; Yang, W.; Gong, W.; Ma, W.; Hou, C.; Li, Y.; Zhang, Q.; Wang, H. Abrasion Resistant/Waterproof Stretchable Triboelectric Yarns Based on Fermat Spirals. *Adv. Mater.* **2021**, *33*, 2100782.
(33) Chen, M.; Wang, Z.; Zhang, Q.; Wang, Z.; Liu, W.; Chen, M.; Wei, L. Self-powered multifunctional sensing based on super-elastic fibers by soluble-core thermal drawing. *Nat. Commun.* **2021**, *12*, 1416.
(34) Sim, H. J.; Choi, C.; Kim, S. H.; Kim, K. M.; Lee, C. J.; Kim, Y. T.; Lepro, X.; Baughman, R. H.; Kim, S. J. Stretchable Triboelectric Fiber for Self-powered Kinematic Sensing Textile. *Sci. Rep.-UK* **2016**, *6*, 35153.
(35) Dong, K.; Hu, Y.; Yang, J.; Kim, S.-W.; Hu, W.; Wang, Z. L. Smart textile triboelectric nanogenerators: Current status and perspectives. *MRS Bull.* **2021**, *46*, 512−521.
(36) He, X.; Zi, Y.; Guo, H.; Zheng, H.; Xi, Y.; Wu, C.; Wang, J.; Zhang, W.; Lu, C.; Wang, Z. L. A Highly Stretchable Fiber-Based Triboelectric Nanogenerator for Self-Powered Wearable Electronics. *Adv. Funct. Mater.* **2017**, *27*, 1604378.
(37) Dong, K.; Deng, J.; Ding, W.; Wang, A. C.; Wang, P.; Cheng, C.; Wang, Y.-C.; Jin, L.; Gu, B.; Sun, B.; Wang, Z. L. Versatile Core-Sheath Yarn for Sustainable Biomechanical Energy Harvesting and Real-Time Human-Interactive Sensing. *Adv. Energy Mater.* **2018**, *8*, 1801114.
(38) Souri, H.; Banerjee, H.; Jusufi, A.; Radacsi, N.; Stokes, A. A.; Park, I.; Sitti, M.; Amjadi, M. Wearable and Stretchable Strain Sensors: Materials, Sensing Mechanisms, and Applications. *Advanced Intelligent Systems* **2020**, *2*, 2000039.
(39) Swanney, M. P.; Ruppel, G.; Enright, P. L.; Pedersen, O. F.; Crapo, R. O.; Miller, M. R.; Jensen, R. L.; Falaschetti, E.; Schouten, J. P.; Hankinson, J. L.; Stocks, J.; Quanjer, P. H. Using the lower limit of normal for the FEV1/FVC ratio reduces the misclassification of airway obstruction. *Thorax* **2008**, *63*, 1046−51.
(40) Bhatt, S. P.; Balte, P. P.; Schwartz, J. E.; Cassano, P. A.; Couper, D.; Jacobs, D. R., Jr; Kalhan, R.; O'Connor, G. T.; Yende, S.; Sanders, J. L.; Umans, J. G.; Dransfield, M. T.; Chaves, P. H.; White, W. B.; Oelsner, E. C. Discriminative Accuracy of FEV1:FVC Thresholds for

https://doi.org/10.1021/acsnano.1c09792
ACS Nano XXXX, XXX, XXX−XXX

COPD-Related Hospitalization and Mortality. *JAMA* **2019**, *321*, 2438−2447.

https://doi.org/10.1021/acsnano.1c09792
ACS Nano XXXX, XXX, XXX−XXX